Engineering Fracture Mechanics 194 (2018) 319–336

Contents lists available at ScienceDirect

Engineering Fracture Mechanics

journal homepage: www.elsevier.com/locate/engfracmech

A path-following technique implemented in a Lagrangian formulation to model quasi-brittle fracture

Nicolás A. Labanda[a,c,*], Sebastián M. Giusti[b,c], Bibiana M. Luccioni[a,c]

[a] Structure Institute, National University of Tucumán, Av. Independencia 1800, San Miguel de Tucumán CP 4000, Argentina
[b] GIDMA, Department of Civil Engineering, Regional Faculty of Córdoba, National Technological University, Maestro M. López esq. Cruz Roja, Córdoba X5016ZAA, Argentina
[c] CONICET, Av. Rivadavia 1917, Buenos Aires, Argentina

ARTICLE INFO

Keywords:
Path-following strategy
Augmented Lagrangian method
Cohesive zone model
Fracture simulation
Extrinsic traction-separation law

ABSTRACT

A path-following strategy based on an energy release criterion is proposed and implemented in an augmented Lagrangian formulation to model localized cohesive cracks. The model is formulated in a rigourous variational framework of continuous spaces. A procedure for the solution of the proposed formulation in a continuous spaces context is also presented. The discrete form of the problem for the implementation within the finite element method is also exposed. The ability and robustness of the proposed method to track equilibrium paths including snap-back phenomenon are analyzed and discussed by means of several numerical tests. The restriction based on an energy release criterion is introduced in the formulation by using a augmented Lagrangian method. The effect of the interpolation order for the Lagrange multiplier (so-called *Lagrange field*), its influence on the proposed constraint equation and the mesh density dependency are studied and illustrated in the numerical simulations. Different crack patterns are analyzed and some recommendations concerning the interpolation degree that should be used for the Lagrangian field to avoid spurious energy release are also included.

1. Introduction

The presence of instabilities expressed in terms of snap-back phenomena is a widespread problem in fracture and damage mechanics. As the failure in certain material becomes more brittle, the softening regime tends to have a positive slope, being the linear elastic fracture mechanics (LEFM) the limit solution. The classical approaches used to simulate non linear response that consist of calculating the displacements corresponding to imposed forces or calculating the forces corresponding to certain displacements can no longer be used to trace the equilibrium path in presence of snap-back [1]. In order to clarify these concepts, let us introduce a very simple schematic example. In Fig. 1, two Force-Displacement responses are presented. The dashed line represents the equilibrium path. The solid line in Fig. 1(a) is the response obtained when the displacement for increasing load is calculated. In this case the equilibrium path placed below the A-B segment (snap-through and snap-back) can-not be captured. The solid line in Fig. 1(b) represents the result obtained when the forces corresponding to an increasing displacement are calculated. In this case, the equilibrium path placed to the left of segments A-B and C-D (snap-back) cannot either be computed.

The first attempts to circumvent this problem were proposed independently by Wempner [2] and later by Riks [3]. Years later, Crisfield [5] and Ramm [4] developed a method where an additional constraint equation, independent from the equilibrium equations, is introduced in a staggered solution scheme. The formulation was applied to structural problems with geometrical non

* Corresponding author at: Structure Institute, National University of Tucumán, Av. Independencia 1800, San Miguel de Tucumán, Argentina.
E-mail address: nlabanda@facet.unt.edu.ar (N.A. Labanda).

https://doi.org/10.1016/j.engfracmech.2018.03.004
Received 17 January 2017; Received in revised form 26 February 2018; Accepted 2 March 2018
Available online 28 March 2018
0013-7944/

Nomenclature

$\boldsymbol{b}$	volumetric forces
$\boldsymbol{C}$	elastic fourth-order tensor
$\boldsymbol{C}^t$	elastic fourth-order tensor evaluated at the pseudo-time t
$\mathbb{C}^t$	elastic matrix evaluated at the pseudo-time t
E	Young's modulus
$\dot{\mathscr{E}}$	elastic potential energy rate
G_c	fracture energy
$\mathscr{G}_1, \mathscr{G}_2, \mathscr{G}_3$	variational functionals
h	characteristic element size
$\mathscr{H}$	higher orders terms in a general expansion
$\boldsymbol{I}_{\mathbb{R}^+}$	indicator function
$\mathbb{J}$	matrix of interpolation functions for jump displacement over the fracture
$\mathbb{K}$	stiffness matrix
$\mathbb{K}^0$	initial stiffness matrix
$\mathbb{K}^T$	updated stiffness matrix
n	actual increment
n_{it}	number of iterations
n_{op}	optimal number of iterations
$\boldsymbol{n}$	normal direction vector to the fracture
$\mathbb{N}$	matrix of interpolation functions for displacements
$\mathbb{L}$	matrix of interpolation functions for Lagrange multipliers
$\overline{\boldsymbol{p}}$	prescribed load
$\mathscr{P}$	external power
$\mathscr{P}^k_{c,d}(\mathscr{I})$	polynomial space of order less than or equal to k in $\mathscr{I}$ and with continuous (c) or discontinuous (d) interpolation
$\mathscr{R}$	residue function
$\mathbb{R}$	discrete version of the residue
t, t', t^*	pseudo-time parameter
$\boldsymbol{t_n}$	normal component of the stress on the fracture
$\boldsymbol{t_t}$	tangential component of the stress on the fracture
$\dot{\mathcal{T}}$	energy release rate
$\dot{\mathcal{T}}_{min}$	pre-defined minimal energy release rate
$\boldsymbol{u}$	displacement field
$\mathcal{V}$	space of kinematically admissible displacements variations
$\mathcal{V}^h$	approximation of the space $\mathcal{V}$
$\mathcal{X}$	space of kinematically admissible Lagrange multipliers variations
$\mathcal{X}^h$	approximation of the space $\mathcal{X}$
$\boldsymbol{\gamma}$	penalty parameter
Γ	fracture domain
Γ^h	mesh boundary
δ_c	critical displacement
δ_{eq}	equivalent displacement
$\delta(\bullet)$	increment of $(\bullet)$ in continuum spaces
$\boldsymbol{\delta}$	supplementary variable
$\boldsymbol{\delta_n}$	normal component of the supplementary variable
$\boldsymbol{\delta_t}$	tangential component of the supplementary variable
$\Delta(\bullet)$	discrete increment of the parameter (or variable) $(\bullet)$
Θ	null matrix
$\boldsymbol{\eta}$	load control parameter
κ	internal variable
$\boldsymbol{\lambda}$	Lagrange multipliers
σ_c	critical tension
$\boldsymbol{\sigma}$	stress Cauchy tensor
ψ	cohesive potential function
$\boldsymbol{\Psi}$	pseudo-potential over the crack
ν	Poison ratio
Ω	elastic body domain
Ω^h	mesh family
$(\bullet)\vert_\circ$	$(\bullet)$ evaluated in (or over) $\circ$
LATIN	LArge Increment TIme
LEFM	Linear Elastic Fracture Mechanics
CMOD	Crack Mouth Opening Displacement
CMSD	Crack Mouth Sliding Displacement

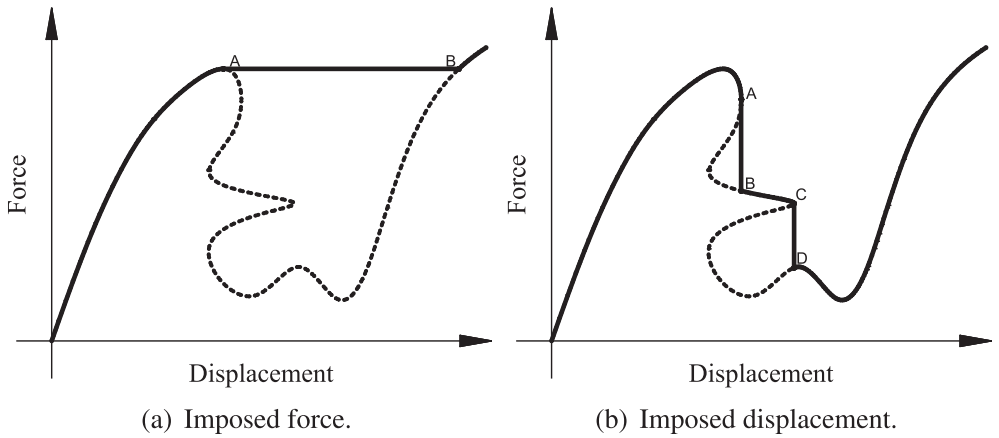

Fig. 1. Computing the equilibrium path.

linearity. However, this kind of formulation failed in the case of problems involving strain localization [6,7].

In the case of material non-linearities, the development of a path-following technique requires additional considerations while formulating the constraint equation. In this sense, Lorentz [24] states a method where the constraint equation is formulated by using

the maximal value of the yield function for the elastic predictor. The novel approach called LATIN method (LArge Increment TIme) proposed in Ref. [20] and expanded in [21–23], departs from the classical step by step scheme used in Newton-Raphson based schemes. It considers an iteration procedure on the entire loading path, but no quadratic convergence behaviour is obtained with this procedure. The widespread criteria proposed by de Borst [7] uses a constraint condition based on the well-known crack mouth opening displacement (CMOD) and the crack mouth sliding displacement (CMSD). The method is capable of tracing the equilibrium path in mixed-mode fracture that occurs in beams and pull-out specimens. This work is considered as the pioneer of the energy-release based path following techniques.

More recently, Gutierrez [8] presented a discussion about an energy release control strategy implemented within the context of a gradient enhanced damage model. Dissipation equation is stated and simultaneously solved with the rest of the equilibrium equations. The method is based on the fact that a fracture involves a monotonically increasing energy dissipation process. Later, an extension of the approach to plasticity and damage with geometrically non-linearity was introduced by Verhoosel et al. [9]. Following the same philosophy, new arc-length functions were developed for a phase field damage model in [1,10,12]. Their implementation in approaches such as damage and fracture modelling for several contexts can be viewed in [11,19] (isogeometric analysis) and [18] (piezoelectric polycrystals), among others.

The methodologies based on Lagrangian functionals and path-following technique to treat damage and fracture mechanics problems have an increasing use in the recent literature [13–16]. However, there are some numerical problems and/or instabilities, such as artificial unloading and spurious energy release that require a detailed treatment. In [17], a continuum formulation was presented where the equivalence between the stationary point of the one-field classic approach and the saddle point of the mixed formulation was proven by solving the double inequality in the continuum space. As a natural extension of the previous work [17], in this paper the formulation is enhanced by combining it with a path-following technique in the context of a Lagrangian formulation to model quasi-brittle fractures. A three-fields formulation is developed within a continuous approach in a rigorous variational framework. The path-following strategy is based on a released energy criterion. This strategy allows controlling the response or tracing the equilibrium path in the material non-linear problems involving cracks evolution.

A constraint equation implemented in an augmented Lagrangian functional to capture snap-back is proposed in this paper for the case of an initially elastic body capable of dissipating energy via a displacement discontinuity driven by a traction-separation law. Basic equilibrium equations for a fractured body under small displacements and small strains are developed following the three-field formulation and they are presented in Section 2. The path following technique is stated starting from an energy analysis, and an additional function to control the fracture process via the released energy is obtained. The finite element discretization, including all the information needed for the computational implementation, is presented in Section 3. Numerical examples are exposed in Section 4, where a discussion about the influence of mesh density on the robustness of the numerical method is presented. The interpolation degree that should be used for the Lagrangian field to avoid spurious energy release in the cases of different crack patterns is also discussed. Finally, the concluding remarks are drawn in Section 5.

2. Variational formulation

2.1. Mixed variational statement for fracture equilibrium problems. Basic equations

The equilibrium approach of the fracture problem consists of a cohesive zone model implemented in a mixed formulation based on an augmented Lagrangian functional. The basic elements of this approach are provided in this work. Further details related to the mathematical foundations can be found in [17]. The functional that describes the energetic behaviour of an infinitesimally deformable body with a discontinuity in the displacement field, as that schematically represented in Fig. 2, can be written as follows:

$$\begin{aligned}\mathscr{G}_1(\boldsymbol{u};\boldsymbol{\lambda}) &= \tfrac{1}{2}\int_{\Omega\setminus\Gamma}\boldsymbol{\sigma}(x,t)\colon\nabla^s\delta\boldsymbol{u}(x,t)\,d\Omega+\int_\Gamma[\boldsymbol{\lambda}+\gamma(\llbracket\boldsymbol{u}\rrbracket-\boldsymbol{\delta})]\cdot\llbracket\delta\boldsymbol{u}\rrbracket\,d\Gamma\\ &\quad-\eta(t)\int_{\partial^t\Omega}\overline{\boldsymbol{p}}(x)\cdot\delta\boldsymbol{u}\,d\partial^t\Omega-\int_{\Omega\setminus\Gamma}\boldsymbol{b}(x,t)\cdot\delta\boldsymbol{u}\,d\Omega\,,\quad\forall\,\delta\boldsymbol{u}\in\mathcal{V},\\ \mathscr{G}_2(\boldsymbol{u};\boldsymbol{\lambda}) &= \int_\Gamma(\llbracket\boldsymbol{u}\rrbracket-\boldsymbol{\delta})\cdot\delta\boldsymbol{\lambda}\,d\Gamma\,,\quad\forall\,\delta\boldsymbol{\lambda}\in\mathcal{X},\end{aligned}\tag{1}$$

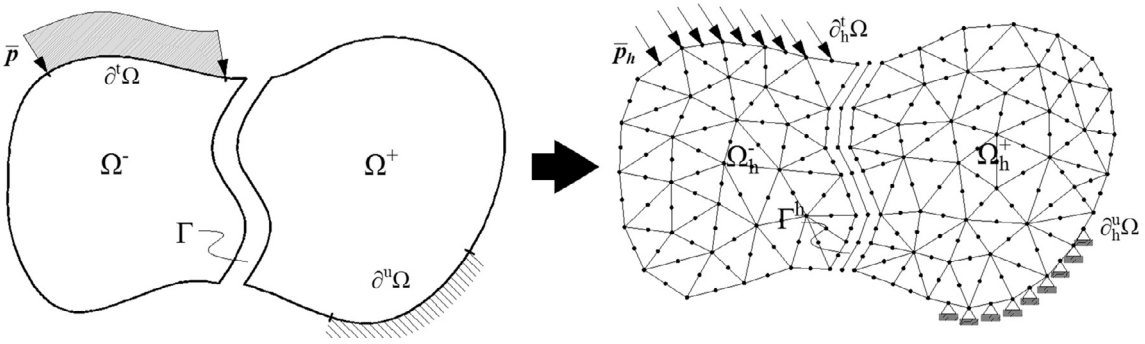

Fig. 2. Domain decomposition of Ω considering a cohesive fracture Γ. Continuum and discrete notation.

where $\partial^t\Omega$ is the Neumann boundary, $\overline{\boldsymbol{p}} \in \boldsymbol{L}^2(\partial^t\Omega)$ is a prescribed load controlled by the parameter η,$\partial^u\Omega$ is the Dirichlet boundary, $\boldsymbol{\sigma}$ is the Cauchy tensor, $\nabla^s\boldsymbol{u}$ denotes the symmetric part of the displacement field gradient, γ is the penalty parameter, $\boldsymbol{\lambda}$ represents the Lagrange multipliers, $\boldsymbol{b} \in \boldsymbol{L}^2(\Omega\backslash\Gamma)$ are the volumetric forces, $[\![\bullet]\!] = (\bullet)|_{\Gamma^+} - (\bullet)|_{\Gamma^-}$ represents the jump of the field $(\bullet)$ over the domain Γ, $\boldsymbol{\delta}$ is a supplementary variable, $\mathcal{V}$ is the space of kinematically admissible displacements variations $\delta\boldsymbol{u}$, and $\mathcal{X}$ is the space of kinematically admissible Lagrange multipliers variations $\delta\boldsymbol{\lambda}$, defined as:

$$\begin{aligned}\mathcal{V}(\Omega\backslash\Gamma) &= \left\{\boldsymbol{v} \in \mathbf{H}^1 \ \wedge \ [\![\boldsymbol{v}]\!] \in \mathbf{H}^{\frac{1}{2}} : \boldsymbol{v}|_{\partial^u\Omega} = 0\right\},\\ \mathcal{X}(\Omega\backslash\Gamma) &= \left\{\boldsymbol{x} | \boldsymbol{x} \in \mathbf{H}^{-\frac{1}{2}}\right\},\end{aligned} \tag{2}$$

Note that the deformable body outside of the discontinuity Γ remains elastic. The functional $\mathscr{G}_1$ in (1) enforces the balance between the internal forces represented by the two first terms and the external forces represented by the last two terms. The functional $\mathscr{G}_2$ weakly enforces the equality $[\![\boldsymbol{u}]\!] = \boldsymbol{\delta}$. The supplementary variable $\boldsymbol{\delta}$ is solved in a staggered scheme motivated by the coordination decomposition method [25] in the so-called collocation points. In this way, the traction-separation law is solved in an inverse way, starting with a predicted Lagrange multiplier field and a displacement field and finally computing the supplementary variable [17]. To this end, the following functional is defined for each collocation point:

$$\mathscr{G}_0(\boldsymbol{u};\boldsymbol{\lambda}) = \boldsymbol{t} - \boldsymbol{\lambda} - \gamma([\![\boldsymbol{u}]\!] - \boldsymbol{\delta}), \quad \boldsymbol{t} \in \partial_{\boldsymbol{\delta}}\Psi(\boldsymbol{\delta},\varkappa). \tag{3}$$

where Ψ is a pseudo-potential over the crack Γ [13]:

$$\Psi([\![\boldsymbol{u}]\!],\varkappa) = \boldsymbol{I}_{\mathbb{R}^+}([\![\boldsymbol{u}]\!]_{\boldsymbol{n}}) + \psi([\![\boldsymbol{u}]\!],\varkappa), \tag{4}$$

with $\boldsymbol{I}_{\mathbb{R}^+}$ an indicator function to avoid the penetration between crack lips in the fracture normal direction $\boldsymbol{n}$, and $\psi: \mathbb{R}^+ \to \mathbb{R}$ representing the cohesive potential function defined in Section 2.2. The operator $\partial_\circ(\cdot)$ represents the sub gradient or generalized derivative of the functional $(\cdot)$ respect to $\circ$. The sub gradient is equal to the partial derivative $\frac{\partial(\cdot)}{\partial\circ}$ only when $(\cdot)$ is differentiable, see [27]. The internal variable $\varkappa$ is used to set the irreversibility nature of the process and it will be defined later. Therefore, the problem is reduced to: *For some* $\gamma \in \mathbb{R}^+$ *and* $\eta \in \mathbb{R}$, *find* $(\boldsymbol{u};\boldsymbol{\lambda}) \in \mathcal{V} \times \mathcal{X}$ *such that*

$$\begin{aligned}\mathscr{G}_1(\boldsymbol{u};\boldsymbol{\lambda}) &= 0\,, \quad \forall\, \delta\boldsymbol{u} \in \mathcal{V},\\ \mathscr{G}_2(\boldsymbol{u};\boldsymbol{\lambda}) &= 0\,, \quad \forall\, \delta\boldsymbol{\lambda} \in \mathcal{X},\end{aligned} \tag{5}$$

where $\boldsymbol{\delta}(\boldsymbol{u};\boldsymbol{\lambda}) \in \ker\mathscr{G}_0(\boldsymbol{u};\boldsymbol{\lambda})$ and $\boldsymbol{u}$ and $\boldsymbol{\lambda}$ are fixed in collocation points.

Note that, due to initial assumptions, the problem under considerations is geometrically linear and the path-following technique, not presented yet, is used to capture complex behaviours related to material non-linearities such as snap-back in the traction-separation response.

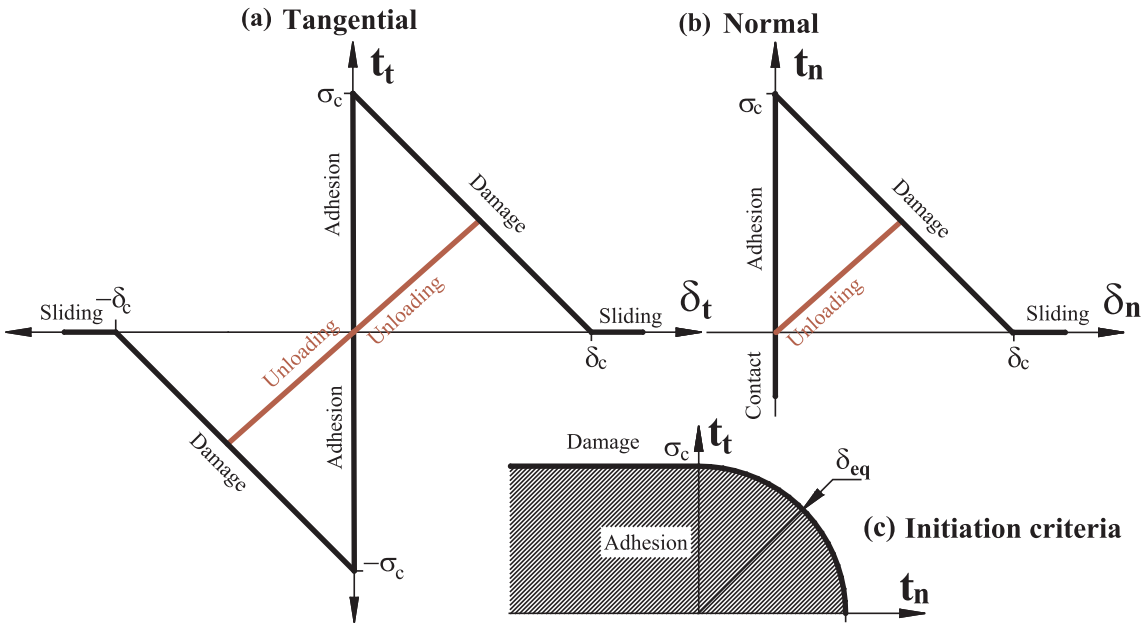

Fig. 3. Traction separation law with linear unloading proposed for the paper. (a) Tangential traction-separation law. (b) Normal traction-separation law. (c) Initiation criteria.

2.2. Traction-separation law

A simple traction-separation law consisting of a linear cohesive zone model that considers contact and adhesion regimes with linear unloading, is used in this paper (see Fig. 3). The potential is defined as follows:

$$\psi(\delta_{eq}) = \begin{cases} G_c \frac{\delta_{eq}}{\delta_c}\left(2-\frac{\delta_{eq}}{\delta_c}\right), & if \quad \delta_{eq} \leqslant \delta_c \\ G_c, & if \quad \delta_{eq} > \delta_c \end{cases}. \tag{6}$$

The parameter $G_c = \frac{1}{2}\sigma_c\delta_c$ is used to denote the fracture energy, σ_c is the critical tension and δ_c is the critical displacement. The potential is totally defined by two of the three parameters (G_c,σ_c,δ_c). The cohesive forces in the crack are driven by an equivalent displacement:

$$\delta_{eq} = \|\boldsymbol{\delta}\| = \sqrt{\boldsymbol{\delta}\cdot\boldsymbol{\delta}}. \tag{7}$$

An irreversible variable κ is introduced to control the crack opening/closure:

$$\kappa(t) = \sup_{t'<t^*} \delta_{eq}(t'); \tag{8}$$

where t^* is the actual time. The initiation criteria used to detect the cracking onset is shown in Fig. 3(c).

2.3. Path-following technique for an augmented Lagrangian formulation

A path following strategy based on a released energy criterion, is developed to control the response. To this end, the load parameter $\eta \in \mathbb{R}$ is introduced as an independent variable. By taking into account the thermodynamics laws, the energy release during the failure is positive and monotonically increasing and its rate can be expressed as follows

$$\mathscr{P} - \dot{\mathscr{E}} = \dot{\mathcal{T}}, \tag{9}$$

where $\mathscr{P}$ is a measure of the power introduced by the external loads, $\dot{\mathscr{E}}$ is the elastic potential energy rate and the difference between them $\dot{\mathcal{T}}$ is a positive function that represents the energy release rate. The elastic potential can be expressed as follows:

$$\mathscr{E} = \frac{1}{2}\left[\int_{\Omega\setminus\Gamma} \boldsymbol{\sigma}(x,t)\colon \nabla^s \boldsymbol{u}(x,t)\, d\Omega\right]. \tag{10}$$

This potential can be also interpreted as the potential inserted by external actions minus the potential dissipated by the system. Applying Green's theorem and taking into account the elastic equilibrium equation:

$$\mathscr{E} = \tfrac{1}{2}\left[\int_{\Omega} \boldsymbol{b}(x,t)\cdot\boldsymbol{u}(x,t)\, d\Omega + \eta(t)\int_{\partial^t\Omega} \overline{\boldsymbol{p}}(x)\cdot\boldsymbol{u}(x,t)\, d\partial^t\Omega - \int_{\Gamma} [\boldsymbol{\lambda} + \gamma\cdot(\llbracket\boldsymbol{u}\rrbracket - \boldsymbol{\delta})]\cdot\llbracket\boldsymbol{u}\rrbracket\, d\Gamma\right]. \tag{11}$$

Note that a penalty term is inserted in the stress projected on the fracture in the above equation to preserve consistency with the formulation. For the sake of simplicity, let us consider no volume forces, then $\dot{\mathscr{E}}$ is given by:

$$\dot{\mathscr{E}} = \tfrac{1}{2}\left[\int_{\partial^t\Omega} [\dot{\eta}\,\hat{p} + \eta\,\dot{\hat{p}}]\, d\partial^t\Omega - \int_{\Gamma} [\dot{\hat{\boldsymbol{\lambda}}}\cdot\llbracket\boldsymbol{u}\rrbracket + \hat{\boldsymbol{\lambda}}\cdot\llbracket\dot{\boldsymbol{u}}\rrbracket]\, d\Gamma\right], \tag{12}$$

where $\hat{\boldsymbol{\lambda}} = \boldsymbol{\lambda} + \gamma(\llbracket\boldsymbol{u}\rrbracket - \boldsymbol{\delta})$ and $\hat{p} = \overline{\boldsymbol{p}}(x)\cdot\boldsymbol{u}$. The power due to external loads is:

$$\mathscr{P} = \eta\left[\int_{\partial^t\Omega} \dot{\hat{p}}\, d\partial^t\Omega\right]. \tag{13}$$

Replacing Eqs. (12) and (13) on the left hand of Eq. (9), the energy release rate can be defined using the following functional $\mathscr{G}_3$:

$$\mathscr{G}_3 = \tfrac{1}{2}\left[\int_{\partial^t\Omega} [\eta\cdot\dot{\hat{p}} - \dot{\eta}\cdot\hat{p}]\, d\partial^t\Omega + \int_{\Gamma} [\dot{\hat{\boldsymbol{\lambda}}}\cdot\llbracket\boldsymbol{u}\rrbracket + \hat{\boldsymbol{\lambda}}\cdot\llbracket\dot{\boldsymbol{u}}\rrbracket]\, d\Gamma\right]. \tag{14}$$

Then the problem controlled by the released energy is stated as: *For some* $\gamma \in \mathbb{R}^+$, *find* $(\boldsymbol{u};\boldsymbol{\lambda};\eta) \in \mathcal{V}\times\mathcal{X}\times\mathbb{R}$ *such that*

$$\begin{aligned} &\mathscr{G}_1(\boldsymbol{u};\boldsymbol{\lambda};\eta) = 0\,, \quad \forall\ \delta\boldsymbol{u} \in \mathcal{V}, \\ &\mathscr{G}_2(\boldsymbol{u};\boldsymbol{\lambda};\eta) = 0\,, \quad \forall\ \delta\boldsymbol{\lambda} \in \mathcal{X}, \\ &\mathscr{G}_3(\boldsymbol{u};\boldsymbol{\lambda};\eta) = \dot{\mathcal{T}}, \end{aligned} \tag{15}$$

where $\dot{\mathcal{T}}$ is the constant predefined energy release rate.

Note that this technique was developed to trace the equilibrium path when the problem under analysis presents non-linearities in the material behaviour. During the simulation, functional $\mathscr{G}_3$ is only activated when a pre-defined fracture criterion, characterized by a initial value of $\dot{\mathcal{T}}$ is reached. If the problem is elastic functional $\mathscr{G}_3$ is null and load or displacement control is used. Moreover, if the simulated problem has a pure elastic regime after a dissipation, the equilibrium path methodology must be switched from the energy release criterion presented here to load or displacement control. A detailed explanation of the procedure solution adopted in this work can be found in the next sections.

2.4. Solution procedure

A strategy to solve the non-linear problem described by Eq. (15) is presented here based on a continuum space approach. First, a Taylor expansion of the functionals $\mathscr{G}_i$, with $i \in [1...3]$ is developed in order to define a residue function $\mathscr{R}$ to be solved in a classical Newton-Raphson scheme. A general expansion of $\mathscr{G}_i$ with respect to the variables $\boldsymbol{u}$,$\boldsymbol{\lambda}$ and η can be written as:

$$\mathscr{G}_i(\boldsymbol{u}|_{n+1};\boldsymbol{\lambda}|_{n+1};\eta|_{n+1}) = \mathscr{G}_i(\boldsymbol{u}|_n;\boldsymbol{\lambda}|_n;\eta|_n) + \overrightarrow{\partial_{\boldsymbol{u}}\mathscr{G}_i}|_n + \overrightarrow{\partial_{\boldsymbol{\lambda}}\mathscr{G}_i}|_n + \overrightarrow{\partial_{\eta}\mathscr{G}_i}|_n + \mathscr{H}, \tag{16}$$

where subindex n indicates the actual increment. The higher orders terms $\mathscr{H}$ in Eq. (16) can be neglected and the directional derivatives $\overrightarrow{\partial_{\boldsymbol{u}}\mathscr{G}_i}, \overrightarrow{\partial_{\boldsymbol{\lambda}}\mathscr{G}_i}$ and $\overrightarrow{\partial_{\eta}\mathscr{G}_i}$ are computed as follows:

$$\overrightarrow{\partial_{\bullet}\mathscr{G}_i} = \lim_{t\to 0^+} \frac{1}{t}[\mathscr{G}_i(\bullet + t\delta\bullet) - \mathscr{G}_i(\bullet)] = \partial_{\bullet}\mathscr{G}_i \cdot \delta\bullet, \tag{17}$$

with $\bullet$ representing any one of the variables $\boldsymbol{u}$,$\boldsymbol{\lambda}$ or η. Now, by replacing $\mathscr{G}_1$ and $\mathscr{G}_2$ in Eq. (17), the following directional derivatives are obtained:

$$\overrightarrow{\partial_{\boldsymbol{u}}\mathscr{G}_1} = \int_{\Omega\setminus\Gamma} \nabla^s\delta\boldsymbol{u} : \boldsymbol{C}^t : \nabla^s\delta\boldsymbol{u}\ d\Omega + \int_\Gamma \gamma\left(\llbracket\delta\boldsymbol{u}\rrbracket - \gamma\ \frac{\partial\delta}{\partial\boldsymbol{t}}\cdot\llbracket\delta\boldsymbol{u}\rrbracket\right)\cdot\llbracket\delta\boldsymbol{u}\rrbracket\ d\Gamma, \tag{18}$$

$$\overrightarrow{\partial_{\boldsymbol{\lambda}}\mathscr{G}_1} = \int_\Gamma \left[\delta\boldsymbol{\lambda} - \gamma\ \frac{\partial\delta}{\partial\boldsymbol{t}}\cdot\delta\boldsymbol{\lambda}\right]\cdot\llbracket\delta\boldsymbol{u}\rrbracket\ d\Gamma, \tag{19}$$

$$\overrightarrow{\partial_{\eta}\mathscr{G}_1} = -\int_{\partial^t\Omega} \overline{\boldsymbol{p}}(x)\cdot\delta\boldsymbol{u}\ d\partial^t\Omega\ \delta\eta, \tag{20}$$

$$\overrightarrow{\partial_{\boldsymbol{u}}\mathscr{G}_2} = \int_\Gamma \left[\llbracket\delta\boldsymbol{u}\rrbracket - \gamma\ \frac{\partial\delta}{\partial\boldsymbol{t}}\cdot\llbracket\delta\boldsymbol{u}\rrbracket\right]\cdot\delta\boldsymbol{\lambda}\ d\Gamma, \tag{21}$$

$$\overrightarrow{\partial_{\boldsymbol{\lambda}}\mathscr{G}_2} = -\int_\Gamma \delta\boldsymbol{\lambda}\cdot\left[\frac{\partial\delta}{\partial\boldsymbol{t}}\cdot\delta\boldsymbol{\lambda}\right] d\Gamma, \tag{22}$$

$$\overrightarrow{\partial_{\eta}\mathscr{G}_2} = 0. \tag{23}$$

To obtain the derivative of $\mathscr{G}_3$, the pseudo temporal increments should be discretized. To this end, an Euler-forward scheme is used. The symbol $(\bullet)|_n$ denotes the converged value of variable $\bullet$ in the previous pseudo-time step and the actual variable is denoted with $(\bullet)$. Therefore, the directional derivatives of $\mathscr{G}_3$ are given by,

$$\overrightarrow{\partial_{\boldsymbol{u}}\mathscr{G}_3} = \frac{1}{2}\left[\eta\Big|_n \int_{\partial^t\Omega} \widehat{\boldsymbol{p}}(\delta\boldsymbol{u})\ d\partial^t\Omega + \int_\Gamma \widehat{\boldsymbol{\lambda}}\Big|_n \cdot\llbracket\delta\boldsymbol{u}\rrbracket\ d\Gamma + \int_\Gamma \gamma\left(\llbracket\delta\boldsymbol{u}\rrbracket - \gamma\ \frac{\partial\delta}{\partial\boldsymbol{t}}\cdot\llbracket\delta\boldsymbol{u}\rrbracket\right)\cdot\llbracket\boldsymbol{u}\rrbracket\Big|_n\ d\Gamma\right], \tag{24}$$

$$\overrightarrow{\partial_{\boldsymbol{\lambda}}\mathscr{G}_3} = \frac{1}{2}\int_\Gamma \left(\delta\boldsymbol{\lambda} - \gamma\ \frac{\partial\delta}{\partial\boldsymbol{t}}\cdot\delta\boldsymbol{\lambda}\right)\cdot\llbracket\boldsymbol{u}\rrbracket\Big|_n\ d\Gamma, \tag{25}$$

$$\overrightarrow{\partial_{\eta}\mathscr{G}_3} = -\frac{1}{2}\int_{\partial^t\Omega} \widehat{\boldsymbol{p}}\Big|_n\ \delta\eta\ d\partial^t\Omega. \tag{26}$$

By replacing the directional derivatives of the continuum functionals $\mathscr{G}_i$, given by Eqs. (18)–(26), in the expansion presented in Eq. (16), a residue $\mathscr{R}$ can be defined as follows:

$$\mathscr{R}(\boldsymbol{u}|_{n+1};\boldsymbol{\lambda}|_{n+1};\eta|_{n+1}) = \begin{Bmatrix} \mathscr{G}_1|_{n+1} - \mathscr{G}_1|_n \\ \mathscr{G}_2|_{n+1} - \mathscr{G}_2|_n \\ \mathscr{G}_3|_{n+1} - \mathscr{G}_3|_n \end{Bmatrix} = \begin{bmatrix} \partial_{\boldsymbol{u}}\mathscr{G}_1 & \partial_{\boldsymbol{\lambda}}\mathscr{G}_1 & \partial_{\eta}\mathscr{G}_1 \\ \partial_{\boldsymbol{u}}\mathscr{G}_2 & \partial_{\boldsymbol{\lambda}}\mathscr{G}_2 & \partial_{\eta}\mathscr{G}_2 \\ \partial_{\boldsymbol{u}}\mathscr{G}_3 & \partial_{\boldsymbol{\lambda}}\mathscr{G}_3 & \partial_{\eta}\mathscr{G}_3 \end{bmatrix}\Bigg|_n \begin{Bmatrix} \delta\boldsymbol{u} \\ \delta\boldsymbol{\lambda} \\ \delta\eta \end{Bmatrix}\Bigg|_{n+1}. \tag{27}$$

It must be remarked that the above coupled problem must be solved when energy dissipation exists. Therefore, the functional $\mathscr{G}_3$ in Eq. (27) is used to enforce the equilibrium path. In the elastic regime, where load or displacement control is used, the problem to be solved can be simplified to:

$$\mathscr{R}(\boldsymbol{u}|_{n+1};\boldsymbol{\lambda}|_{n+1}) = \begin{Bmatrix} \mathscr{G}_1|_{n+1} - \mathscr{G}_1|_n \\ \mathscr{G}_2|_{n+1} - \mathscr{G}_2|_n \end{Bmatrix} = \begin{bmatrix} \partial_{\boldsymbol{u}}\mathscr{G}_1 & \partial_{\boldsymbol{\lambda}}\mathscr{G}_1 \\ \partial_{\boldsymbol{u}}\mathscr{G}_2 & \partial_{\boldsymbol{\lambda}}\mathscr{G}_2 \end{bmatrix}\Bigg|_n \begin{Bmatrix} \delta\boldsymbol{u} \\ \delta\boldsymbol{\lambda} \end{Bmatrix}\Bigg|_{n+1}, \tag{28}$$

The simulation begins with a load (or displacement) control methodology characterized by the residue (28). When the released energy reaches a pre-defined threshold $\dot{\mathscr{T}}_0$, the path following technique is introduced and the residue is expanded to calculate η taking into account functional $\mathscr{G}_3$, defined in Eq. (27). For successive loads steps, the following criterion is used to estimate an appropriate value for the release energy rate

$$\dot{\mathcal{T}}\Big|_{n+1} = \dot{\mathcal{T}}\Big|_{n} \frac{n_{op}}{n_{it}|_n}, \tag{29}$$

where $n_{it}|_n$ and $\dot{\mathcal{T}}|_n$ are the number of iterations and the released energy rate of the last converged load step, respectively. The parameter n_{op} is the *optimal number of iterations* and it must be defined for each problem. If the energy release rate in an iteration is below a certain pre-defined value $\dot{\mathcal{T}}_{min}$, it is assumed that the problem is within an elastic regime. Under this situation, the strategy based on the functional $\mathscr{G}_3$ is avoided and the problem to be solved is contracted to (28), where a load (or displacement) control technique is activated.

The problem based on the residues presented above is numerically solved in the context of the finite element method. The main elements needed for the discretization are presented in the next section.

3. Finite element implementation

Let $\Omega^h|_{h>0}$ be a mesh family that converges exactly to Ω, where $h > 0$ is the characteristic element size, and let $\Gamma^h|_{h>0}$ be the set of the mesh boundary that converges exactly to Γ. By considering a polynomial discretization of the domain, characterized by the parameter $h > 0$, the spaces $\mathscr{V}^h$ and $\mathscr{Z}^h$ are the approximations of the continuum spaces presented in Eq. (2), where the supra-index h is used to denote its discrete version. Therefore, the spaces $\mathscr{V}^h$ and $\mathscr{Z}^h$ can be expressed in a discrete manner as:

$$\mathscr{V}^h = \mathscr{P}^2_c(\Omega^h) \quad \text{and} \quad \mathscr{Z}^h = \mathscr{P}^k_{c,d}(\Gamma^h), \tag{30}$$

where $\mathscr{P}^k_{c,d}(\mathscr{I})$ denotes a polynomial space of order less than or equal to k in $\mathscr{I}$ and the sub-indexes c and d represent a continuous or discontinuous interpolation, respectively. Taking into account the above approximation, the displacement field $\boldsymbol{u}$, the strain field $\boldsymbol{\varepsilon}$ and the Lagrange multiplier $\boldsymbol{\lambda}$ can be written as:

$$\boldsymbol{u}(\boldsymbol{x},t) \approx \boldsymbol{u}^h = [\mathbb{N}(\boldsymbol{x},t)]\{\boldsymbol{U}\} \Rightarrow \delta\boldsymbol{u} \approx \delta\boldsymbol{u}^h = [\mathbb{N}(\boldsymbol{x},t)]\{\delta\boldsymbol{U}\}, \tag{31}$$

$$\boldsymbol{\varepsilon}(\boldsymbol{x},t) = \nabla^s\boldsymbol{u} \approx \nabla^s\boldsymbol{u}^h = [\nabla^s\mathbb{N}(\boldsymbol{x},t)]\cdot\{\boldsymbol{U}\}, \tag{32}$$

$$\boldsymbol{\lambda}(\boldsymbol{x},t) \approx \boldsymbol{\lambda}^h = [\mathbb{L}(\boldsymbol{s},t)]\cdot\{\boldsymbol{\Lambda}\} \Rightarrow \delta\boldsymbol{\lambda} \approx \delta\boldsymbol{\lambda}^h = [\mathbb{L}(\boldsymbol{s},t)]\cdot\{\delta\boldsymbol{\Lambda}\}, \tag{33}$$

being $\mathbb{N}(\boldsymbol{x},t)$ the matrix of interpolation functions for displacements and $\mathbb{L}(\boldsymbol{s},t)$ the matrix of interpolation functions for Lagrange multipliers. The matrix $\mathbb{J}(\boldsymbol{s},t) = \check{\mathbb{N}}_+(\boldsymbol{s},t) - \check{\mathbb{N}}_-(\boldsymbol{s},t)$ is a *jump operator* that maps the displacement field $\boldsymbol{u}$ to the gap field $[\![\boldsymbol{u}]\!]$ and it is introduced as follows:

$$[\![\boldsymbol{u}(\boldsymbol{s},t)]\!] \approx [\![\boldsymbol{u}^h]\!] = [\check{\mathbb{N}}_+(\boldsymbol{s},t) - \check{\mathbb{N}}_-(\boldsymbol{s},t)]\cdot\{\boldsymbol{U}\} = [\mathbb{J}(\boldsymbol{s},t)]\cdot\{\boldsymbol{U}\}, \tag{34}$$

where $\check{\mathbb{N}}_+$ and $\check{\mathbb{N}}_-$ are computed as the bulk shape function particularized in both sides of the crack lips. Consequently

$$[\![\delta\boldsymbol{u}]\!] \approx [\![\delta\boldsymbol{u}^h]\!] = [\mathbb{J}(\boldsymbol{s},t)]\cdot\{\delta\boldsymbol{U}\}. \tag{35}$$

Replacing Eqs. (31)–(34) into Eq. (27), the following relation is obtained:

$$\mathbb{R}(\boldsymbol{u}|_{n+1};\boldsymbol{\lambda}|_{n+1};\eta|_{n+1}) = \begin{bmatrix} \mathbb{K}_{\boldsymbol{uu}} & \mathbb{K}_{\boldsymbol{u\lambda}} & \mathbb{K}_{\boldsymbol{u}\eta} \\ \mathbb{K}_{\boldsymbol{\lambda u}} & \mathbb{K}_{\lambda\lambda} & \mathbb{K}_{\lambda\eta} \\ \mathbb{K}_{\eta\boldsymbol{u}} & \mathbb{K}_{\eta\lambda} & \mathbb{K}_{\eta\eta} \end{bmatrix}\Bigg|_n \begin{Bmatrix} \delta\boldsymbol{U} \\ \delta\boldsymbol{\Lambda} \\ \delta\eta \end{Bmatrix}\Bigg|_{n+1} = [\mathbb{K}]|_n \{\delta\boldsymbol{X}\}\Big|_{n+1}. \tag{36}$$

The stiffness matrix $\mathbb{K}$ is splitted in an initial matrix $\mathbb{K}^0$ (computed during the pre process of the finite element method solver), and $\mathbb{K}^T$ (updated in each iteration), as follows

$$\mathbb{K} = \mathbb{K}^0 + \mathbb{K}^T = \begin{bmatrix} \mathbb{K}^0_{\boldsymbol{uu}} & \mathbb{K}^0_{\boldsymbol{u\lambda}} & \mathbb{K}^0_{\boldsymbol{u}\eta} \\ \mathbb{K}^0_{\boldsymbol{\lambda u}} & \mathbb{K}^0_{\lambda\lambda} & \mathbb{K}^0_{\lambda\eta} \\ \mathbb{K}^0_{\eta\boldsymbol{u}} & \mathbb{K}^0_{\eta\lambda} & \mathbb{K}^0_{\eta\eta} \end{bmatrix} + \begin{bmatrix} \mathbb{K}^T_{\boldsymbol{uu}} & \mathbb{K}^T_{\boldsymbol{u\lambda}} & \mathbb{K}^T_{\boldsymbol{u}\eta} \\ \mathbb{K}^T_{\boldsymbol{\lambda u}} & \mathbb{K}^T_{\lambda\lambda} & \mathbb{K}^T_{\lambda\eta} \\ \mathbb{K}^T_{\eta\boldsymbol{u}} & \mathbb{K}^T_{\eta\lambda} & \mathbb{K}^T_{\eta\eta} \end{bmatrix}. \tag{37}$$

Following the notation presented in Fig. 2, the sub-matrices of the initialization matrix $\mathbb{K}^0$ are explicitly expressed as:

$$\mathbb{K}^0_{\boldsymbol{uu}} = \int_{\Omega^h\setminus\Gamma^h} [\nabla^s\mathbb{N}(\boldsymbol{x},t)]^T [\mathbb{C}^t] [\nabla^s\mathbb{N}(\boldsymbol{x},t)]\, d\Omega^h + \int_{\Gamma^h} \gamma\, [\mathbb{J}(\boldsymbol{s},t)]^T [\mathbb{J}(\boldsymbol{s},t)]\, d\Gamma^h, \tag{38}$$

$$\mathbb{K}^0_{\boldsymbol{u\lambda}} = \int_{\Gamma^h} [\mathbb{L}(\boldsymbol{s},t)]^T\, [\mathbb{J}(\boldsymbol{s},t)]\, d\Gamma^h, \tag{39}$$

$$\mathbb{K}^0_{\boldsymbol{\lambda u}} = \int_{\Gamma^h} [\mathbb{J}(\boldsymbol{s},t)]^T\, [\mathbb{L}(\boldsymbol{s},t)]\, d\Gamma^h, \tag{40}$$

$$\mathbb{K}^0_{\lambda\lambda} = \Theta;\ \ \mathbb{K}^0_{\boldsymbol{u}\eta} = \Theta;\ \ \mathbb{K}^0_{\lambda\eta} = \Theta;\ \mathbb{K}^0_{\eta\eta} = \Theta;\ \mathbb{K}^0_{\eta\boldsymbol{u}} = \Theta;\ \ \mathbb{K}^0_{\eta\lambda} = \Theta, \tag{41}$$

being Θ the null matrix. Observe that the above components of the stiffness matrix are fixed in the overall simulation. The components of the matrix $\mathbb{K}^T$ are computed as:

$$\mathbb{K}^T_{\boldsymbol{uu}} = -\int_{\Gamma^h} \gamma^2\ [\mathbb{J}(\boldsymbol{s},t)]^T \left[\frac{\partial \boldsymbol{\delta}}{\partial \boldsymbol{t}}\right] [\mathbb{J}(\boldsymbol{s},t)]\ d\Gamma^h, \tag{42}$$

$$\mathbb{K}^T_{\boldsymbol{u\lambda}} = -\int_{\Gamma^h} \gamma\ [\mathbb{L}(\boldsymbol{s},t)]^T \left[\frac{\partial \boldsymbol{\delta}}{\partial \boldsymbol{t}}\right] [\mathbb{J}(\boldsymbol{s},t)]\ d\Gamma^h, \tag{43}$$

$$\mathbb{K}^T_{\boldsymbol{u\eta}} = -\int_{\partial^t_h\Omega} [\mathbb{N}(\boldsymbol{x},t)]^T \{\overline{\boldsymbol{p}}\}\ d\partial^t_h\Omega, \tag{44}$$

$$\mathbb{K}^T_{\boldsymbol{\lambda u}} = -\int_{\Gamma^h} \gamma\ [\mathbb{J}(\boldsymbol{s},t)]^T \left[\frac{\partial \boldsymbol{\delta}}{\partial \boldsymbol{t}}\right] [\mathbb{L}(\boldsymbol{s},t)]\ d\Gamma^h, \tag{45}$$

$$\mathbb{K}^T_{\boldsymbol{\lambda\lambda}} = -\int_{\Gamma^h} [\mathbb{L}(\boldsymbol{s},t)]^T \left[\frac{\partial \boldsymbol{\delta}}{\partial \boldsymbol{t}}\right] [\mathbb{L}(\boldsymbol{s},t)]\ d\Gamma^h, \tag{46}$$

$$\mathbb{K}^T_{\boldsymbol{\lambda\eta}} = \Theta, \tag{47}$$

$$\mathbb{K}^T_{\boldsymbol{\eta u}} = \frac{1}{2}\left[\eta\Big|_n \int_{\partial^t_h\Omega} \{\overline{\boldsymbol{p}}\}^T[\mathbb{N}(\boldsymbol{x},t)]\ d\partial^t_h\Omega + \int_{\Gamma^h} \{\hat{\boldsymbol{\lambda}}^h|_n\}^T\ [\mathbb{J}(\boldsymbol{s},t)]\ d\Gamma + \{\boldsymbol{u}^h|_n\}^T\left(\int_{\Gamma^h}\gamma\ [\mathbb{J}(\boldsymbol{s},t)]^T[\mathbb{J}(\boldsymbol{s},t)]\ d\Gamma^h + \mathbb{K}^T_{\boldsymbol{uu}}\right)\right], \tag{48}$$

$$\mathbb{K}^T_{\boldsymbol{\eta\lambda}} = \frac{1}{2}\{\boldsymbol{u}^h|_n\}^T[\mathbb{K}^0_{\boldsymbol{u\lambda}} + \mathbb{K}^T_{\boldsymbol{u\lambda}}], \tag{49}$$

$$\mathbb{K}^T_{\boldsymbol{\eta\eta}} = -\frac{1}{2}\left\{\int_{\partial^t_h\Omega} \{\overline{\boldsymbol{p}}\}\ \ d\partial^t_h\Omega\right\}^T \{\boldsymbol{u}^h|_n\}. \tag{50}$$

Note that the matrix $\left[\frac{\partial \boldsymbol{\delta}}{\partial \boldsymbol{t}}\right]$ is the only element in $\mathbb{K}^T$ that must be updated in each iteration and it is explicitly calculated in Ref. [17]. In order to keep the work self-contained the procedure is presented in Algorithm 1.

Algorithm 1. Constitutive model integration

Input: $\kappa, \gamma\ \sigma_c, \delta_c, \boldsymbol{\lambda}|_n, [\![\boldsymbol{u}]\!]|_n$

Output: $\boldsymbol{\delta}|_{n+1}\ \frac{\partial \boldsymbol{\delta}}{\partial \boldsymbol{t}}\Big|_{n+1}$

$\widetilde{\boldsymbol{t}}|_n = \boldsymbol{\lambda}|_n + \gamma \cdot [\![\boldsymbol{u}]\!]|_n$
if $\kappa = 0$ and $\|\widetilde{\boldsymbol{t}}|_n\|_+ \leqslant \sigma_c$ **then**
  $\boldsymbol{\delta}|_{n+1} = 0$ (Perfect adhesion)
else if $\kappa > 0$ and $\|\widetilde{\boldsymbol{t}}|_n\|_+ \leqslant \gamma\cdot\kappa + \psi'(\kappa)$ **then**
  $\boldsymbol{\delta}\Big|_{n+1} = \frac{\langle \widetilde{\boldsymbol{t}}|_n\rangle_+}{\gamma + \frac{\psi'(\kappa)}{\kappa}}$ (Unloading)
else if $\kappa > 0$ and $\gamma\cdot\kappa + \psi'(\kappa) < \|\widetilde{\boldsymbol{t}}|_n\|_+$ **then**
  $\boldsymbol{\delta}\Big|_{n+1} = \delta_{eq}\cdot\frac{\langle \widetilde{\boldsymbol{t}}|_n\rangle_+}{\|\widetilde{\boldsymbol{t}}|_n\|_+}$; δ_{eq} Solution of $\psi'(\delta_{eq}) + \gamma\cdot\delta_{eq} - \|\widetilde{\boldsymbol{t}}|_n\|_+ = 0$ (Damage)
end if
Derivative of $\boldsymbol{\delta}$ in $\widetilde{\boldsymbol{t}}$
if $\widetilde{t_n}|_n \geqslant 0$ (Tension) **then**
  if $\kappa = 0$ and $\|\widetilde{\boldsymbol{t}}|_n\|_+ \leqslant \sigma_c$ **then** (Perfect adhesion)
    $\frac{\partial \boldsymbol{\delta}}{\partial \boldsymbol{t}}\Big|_{n+1} = \Theta_{2x2}$
  else if $\kappa > 0$ and $\|\widetilde{\boldsymbol{t}}|_n\|_+ \leqslant \gamma\cdot\kappa + \psi'(\kappa)$ **then**(Unloading)
    $\frac{\partial \boldsymbol{\delta}}{\partial \boldsymbol{t}}\Big|_{n+1} = \frac{1}{\gamma + \frac{\psi'(\kappa)}{\kappa}}\mathbb{I}$
  else if $\kappa > 0$ and $\gamma\cdot\kappa + \psi'(\kappa) < \|\widetilde{\boldsymbol{t}}|_n\|_+$ **then** (Damage)
    if $\delta_{eq} \leqslant \delta_c$ **then**
      $\frac{\partial \boldsymbol{\delta}}{\partial \boldsymbol{t}}\Big|_{n+1} = \frac{\delta_{eq}}{\|\widetilde{\boldsymbol{t}}|_n\|_+}\left[\mathbb{I} - \frac{\widetilde{\boldsymbol{t}}|_n}{\|\widetilde{\boldsymbol{t}}|_n\|_+}\otimes\frac{\widetilde{\boldsymbol{t}}|_n}{\|\widetilde{\boldsymbol{t}}|_n\|_+}\right] + \left[\frac{\partial}{\partial \widetilde{\boldsymbol{t}}}\delta_{eq}\right]\otimes\frac{\langle \widetilde{\boldsymbol{t}}|_n\rangle_+}{\|\widetilde{\boldsymbol{t}}|_n\|_+}$; δ_{eq} Solution of $\psi'(\delta_{eq}) + \gamma\cdot\delta_{eq} - \|\widetilde{\boldsymbol{t}}|_n\|_+ = 0$
    else if $\delta_{eq} > \delta_c$ **then**
      $\frac{\partial \boldsymbol{\delta}}{\partial \boldsymbol{t}}\Big|_{n+1} = \frac{1}{\gamma}\mathbb{I}$
    end if

20: **end if**
21: **end if** $\widetilde{t}_n|_n < 0$ (Compression) **then**
22: **if** $\kappa = 0$ and $\|\widetilde{\boldsymbol{t}}|_n\|_+ \leqslant \sigma_c$ **then** (Perfect adhesion)
23: $\left.\frac{\partial \delta}{\partial \boldsymbol{t}}\right|_{n+1} = \Theta_{2x2}$
24: **else if** $\kappa > 0$ and $\|\widetilde{\boldsymbol{t}}|_n\|_+ \leqslant \gamma{\cdot}\kappa + \psi'(\kappa)$ **then**(Unloading)
25: $\left.\frac{\partial \delta}{\partial \boldsymbol{t}}\right|_{n+1} = \frac{1}{\gamma + \frac{\psi'(\kappa)}{\kappa}}(\mathbb{I} - \boldsymbol{n} \otimes \boldsymbol{n})$
26: **else if** $\kappa > 0$ and $\gamma{\cdot}\kappa + \psi'(\kappa) < \|\widetilde{\boldsymbol{t}}|_n\|_+$ **then** (Damage)
27: **if** $\delta_{eq} \leqslant \delta_c$ **then**
28: $\left.\frac{\partial \delta}{\partial \boldsymbol{t}}\right|_{n+1} = \left[\frac{\partial}{\partial \widetilde{\boldsymbol{t}}}\delta_{eq}\right] \otimes \frac{\langle \widetilde{\boldsymbol{t}}|_n \rangle_+}{\|\widetilde{\boldsymbol{t}}|_n\|_+} : \delta_{eq}$ Solution of $\psi'(\delta_{eq}) + \gamma{\cdot}\delta_{eq} - \|\widetilde{\boldsymbol{t}}|_n\|_+ = 0$
29: **else if** $\delta_{eq} > \delta_c$ **then**
30: $\left.\frac{\partial \delta}{\partial \boldsymbol{t}}\right|_{n+1} = \frac{1}{\gamma}(\mathbb{I} - \boldsymbol{n} \otimes \boldsymbol{n})$
31: **else if**
32: **else if**
33: **else if**

The simulation in the elastic regime must be started with a load or displacement control for the calculation of the residue:

$$\mathbb{R}(\boldsymbol{u}|_{n+1}; \boldsymbol{\lambda}|_{n+1}) = \left[\begin{matrix} \mathbb{K}_{\boldsymbol{uu}} & \mathbb{K}_{\boldsymbol{u\lambda}} \\ \mathbb{K}_{\boldsymbol{\lambda u}} & \mathbb{K}_{\boldsymbol{\lambda\lambda}} \end{matrix}\right]\Bigg|_n \cdot \left\{\begin{matrix} \delta \boldsymbol{U} \\ \delta \boldsymbol{\Lambda} \end{matrix}\right\}\Bigg|_{n+1} \tag{51}$$

where $\mathbb{R}$ is the discrete version of the residue formulated in (28). When the path-following is activated, the stiffness matrix is expanded to calculate η as defined in Eq. (36).

4. Numerical tests

For the numerical simulations presented in this section, a load-displacement control based on a controlled incremental parameter was used. A prescribed parameter η is applied in the boundary conditions and its value is updated in each increment during the elastic stage. The simulation begins by setting the control parameter in $\eta = 1 \times 10^{-4}$ and the updating rule is $\eta|_{n+1} = \eta|_n + \Delta\eta$ with

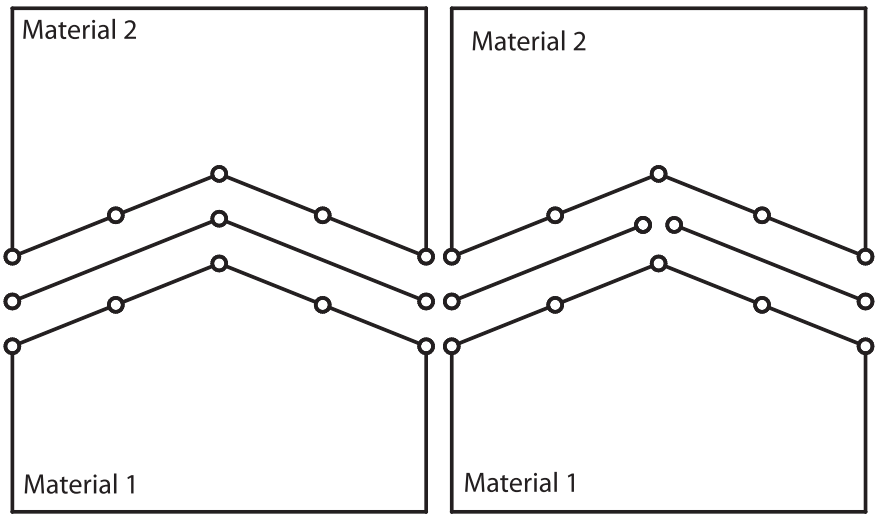

(a) Schematic plot for a first order continuous interpolation $\mathscr{X}^h = \mathcal{P}^1_c\left(\Gamma^h\right)$ in Lagrangian field.

(b) Schematic plot for a first order discontinuous interpolation $\mathscr{X}^h = \mathcal{P}^1_d\left(\Gamma^h\right)$ in Lagrangian field.

Fig. 4. Spurious energy dissipation. Tortuous fracture.

$\Delta\eta = 5 \times 10^{-5}$. The released energy threshold is $\dot{\mathcal{T}}_0 = 2 \times 10^{-5}$ [Nmm], the minimal value of the released energy rate is $\dot{\mathcal{T}}_{min} = 1 \times 10^{-8}$ [N mm] and the parameter related to the optimal number of iterations is $n_{op} = 9$, following the recommendations of Ref. [9]. When the elastic stage appears after a dissipation, typically in snap-back phenomena, and load or displacement control needs to be activated (following the procedure indicated in Section 2.4), the initial value of η to be considered for the control is the last converged value from the previous dissipation stage.

4.1. Lagrange field interpolation to avoid spurious energy dissipation

Some considerations about the interpolation order of the Lagrangian field must be made. Two examples are presented as illustration. The first numerical example is a simple test with a tortuous fracture where two different interpolations are chosen. A first order continuous interpolation $\mathscr{X}^h = \mathscr{P}_c^1(\Gamma^h)$ in the Lagrangian field showed in Fig. 4(a) and a first order discontinuous interpolation $\mathscr{X}^h = \mathscr{P}_d^1(\Gamma^h)$ in the Lagrangian field showed in Fig. 4(b) are considered. Material properties are presented in Table 1. A 1000 [mm] side square is subjected to an uniaxial load in vertical direction. The problem is solved by using 43 load steps.

Results are presented in Fig. 5 where the variation of $\mathscr{G}_3$ in each load step is plotted. In the first case where $\mathscr{X}^h = \mathscr{P}_c^1(\Gamma^h)$, a spurious energy release dissipation in the elastic regime, with a strong dependency of the slope on the value of the penalty parameter γ, reaching values of 5 [N mm] approximately, can be observed in Fig. 5(a). When a discontinuous interpolation is used, the dissipation in the elastic stage is negligible, corresponding to a residual value in the order of 1×10^{-11} [N mm].

For the second example, the debonding of a stiffer fiber from a softer matrix is analyzed. The structural configuration and boundary conditions are presented in Fig. 6(a), where a unitary value of the prescribed uniformly distributed forces f_p is considered. The material properties are presented in Table 1. The problem is solved by using 42 load steps. Using a first order continuous interpolation $\mathscr{X}^h = \mathscr{P}_c^1(\Gamma^h)$ for the Lagrangian field, a spurious dissipation is once again observed in the elastic regime (Fig. 7(a)). When a second order continuous interpolation $\mathscr{X}^h = \mathscr{P}_c^2(\Gamma^h)$ is used for the Lagrangian field (Fig. 6(b)), this problem is avoided and no spurious dissipation is observed, see Fig. 7(b). For the case represented in Fig. 6(b), the energy dissipation rate in the elastic stage is in the order of the residual, being around $\times 10^{-10}$ [N mm] times of the value obtained for the Lagrangian space $\mathscr{X}^h = \mathscr{P}_c^1(\Gamma^h)$.

The numerical examples presented in this section show the main limitation of the presented method. A correct interpolation order of the Lagrangian space must be chosen in each fracture case, proving that the released energy rate during the elastic stage is in the order of the residue.

4.2. Mesh sensitivity of the proposed method

The following example is proposed to study the kindness of the numerical method to find by itself a simple crack path even when an instability in its propagation occurs. Additionally, this example is used to analyse the sensitivity of the path following technique to the mesh density. A sample of 47.5 μm side including a notch and consisting of 20 grains joined by interfaces is analysed (see Fig. 8(a)). The geometry is generated using the algorithm presented by Talischi et al. [26]. The structural configuration and the displacement boundary conditions considered are presented in Fig. 8(a), where u_p is a unitary value. The elastic parameters used for the grains are: $E = 75{,}000$ [MPa] for Young's modulus and $\nu = 0.34$ for Poison ratio. The elastic threshold used for the interface is $\sigma_c = 5000$ [MPa] and different values for the fracture energy are considered. Three cell discretization consisting of triangle elements with 6 nodes (T6) for bulk and linear elements with two nodes (L2) for the interfaces are proposed for this case (see Fig. 8(b-d)). The properties of the three meshes are presented in Table 2. The number of load steps needed during the simulation is 203 (for Mesh N°1), 1424 (for Mesh N°2) and 1264 (for Mesh N°3).

The results of the proposed examples are plotted in Fig. 9, where the displacement corresponds to the top-right corner and the force is the summation of the top edge reactions. The force-displacement curve for a fracture energy of $G_c = 0.001$ J/mm^2 obtained with the three proposed meshes are presented in Fig. 9(a). It can be seen that for the coarser meshes, N°1 and N°2, the curves present an intermittent behaviour between snap back and forward, losing the convergence in the first case. For the finer meshes N°2 and N°3 the convergence was achieved. This fact is due to the cohesive length of the cohesive law not being resolved for the mesh N°1. A method to avoid this phenomenon is presented in Refs. [28,29], where the adequate finite element size is determined based on the constitutive properties of the materials. The mentioned effect is not observed when higher fracture energy values are used. For instance, in Fig. 9(b) the results obtained for the same numerical example but using $G_c = 0.004$ J/mm^2 are shown. The response curves present a smother behaviour for all meshes. A strong dependence of the released energy rate functional $\mathscr{G}_3$ on the mesh density is detected.

Table 1
Material properties.

	Material 1	Material 2	Interface
E [MPa]	3900	86,900	–
Poisson mod.	0.37	0.23	–
σ_c [MPa]	–	–	30
G_c [N/mm]	–	–	30

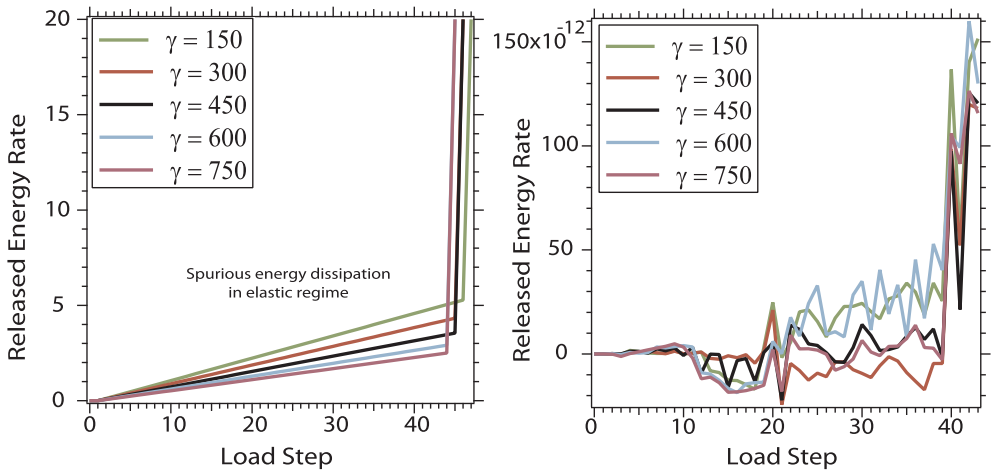

(a) Results for a first order continuous interpolation $\mathscr{X}^h = \mathscr{P}_c^1\left(\Gamma^h\right)$ in Lagrangian field. (b) Results for a first order discontinuous interpolation $\mathscr{X}^h = \mathscr{P}_d^1\left(\Gamma^h\right)$ in Lagrangian field.

Fig. 5. Released energy rate in tortuous fracture.

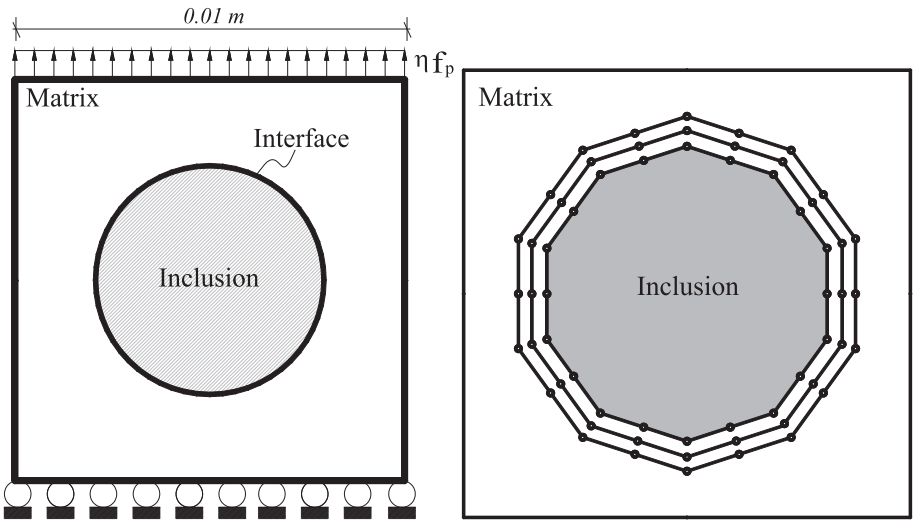

(a) Structural configuration. (b) Schematic plot for a second order interpolation $\mathscr{X}^h = \mathscr{P}_c^2\left(\Gamma^h\right)$ in Lagrangian field.

Fig. 6. Proposed example for spurious energy dissipation analysis. Fibre-matrix debonding.

4.3. Perforated double cantilever beam

The following example has been proposed in Ref. [9] and it has been reproduced by other researchers [1,19,23] to simulate brittle behaviour of a crack propagation. The objective of this example is the study of the proposed path-following method in the augmented Lagrangian context. The proposed structure presented in Fig. 10 is a double cantilever beam with equally-spaced perforations and unitary opposite displacements at the left corners, i.e. $u_p = 1$ [mm]. In this structural configuration it is expected that the propagating crack produces a snap-back in the force-displacement response. The beam is discretized using 1866 8-nodes quadrilateral (Q8) elements with nine gauss points for bulk and 120 2-nodes linear elements (L2) with two gauss points for the interface. The Young's modulus is $E = 100$ [N/mm^2], the Poison's ratio is $\nu = 0.3$ and the critical tension is $\sigma_c = 1$ [N/mm^2]. The problem is solved after 470 load steps and 1860 total iterations.

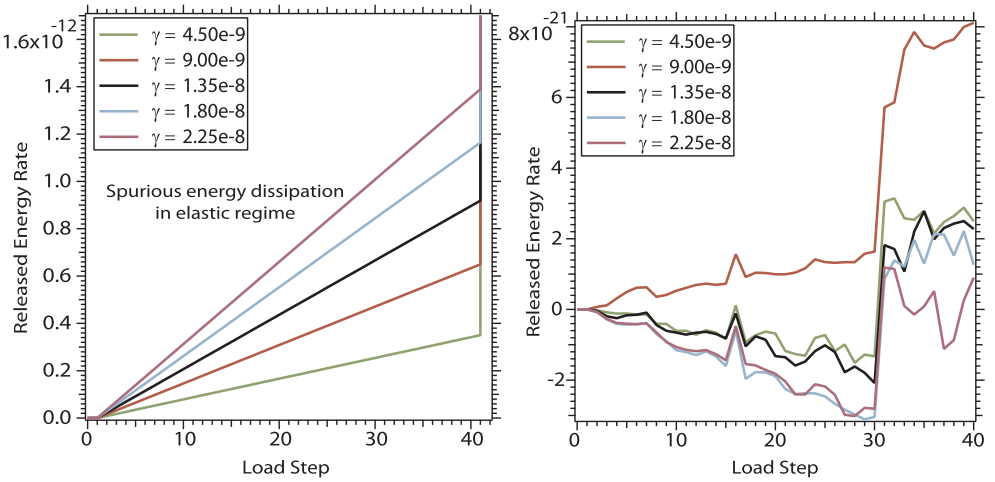

(a) Results for a first order continuous interpolation $\mathscr{X}^h = \mathcal{P}_c^1\left(\Gamma^h\right)$ in Lagrangian field. (b) Results for a second order continuous interpolation $\mathscr{X}^h = \mathcal{P}_c^2\left(\Gamma^h\right)$ in Lagrangian field.

Fig. 7. Results for spurious energy dissipation example based in a fibre-matrix debonding.

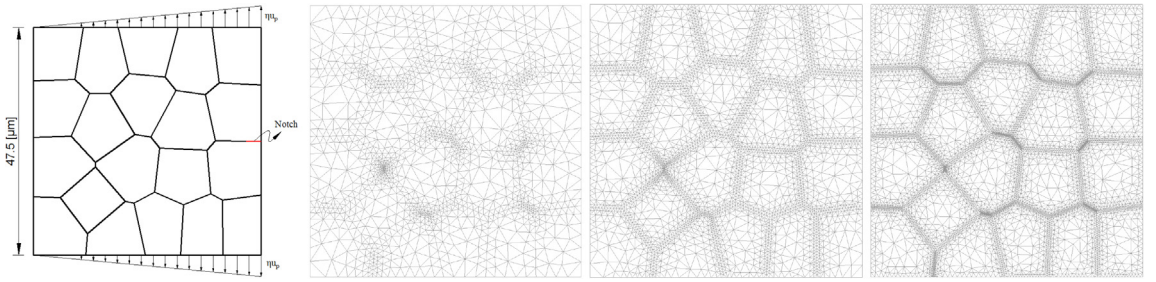

(a) Mesh N°1. (b) Mesh N°1. (c) Mesh N°2. (d) Mesh N°3.

Fig. 8. Inter-granular fracture problem. Proposed polycrystal cell.

Table 2
Mesh properties used for polycrystal.

	Min [μm]	Max [μm]	N° T6	N° L2
Mesh 1	0.137	1.78	2623	381
Mesh 2	0.137	0.521	6114	680
Mesh 3	0.0319	0.39	13194	1260

Figs. 11 and 12 show the obtained results for a fracture energy of $G_c = 0.0025$ [N/mm]. The force-displacement curve is plotted in Fig. 11(a), showing a behaviour similar to that presented in other papers [9,23,10]. It can be seen that the crack instability, i.e. the activation of the abrupt crack propagation in each solid segment, depends on its location in the structure with respect to the load position (Fig. 14). The total released energy $\mathcal{T}$ versus the displacement is plotted in Fig. 11(b). The jumps of the released energy at the ends of each instability are clearly equal to the release energy in each segment between the holes, e.g. $\Delta\mathcal{T}_{A-B} = 0.175 \cdot [\text{mm}] \cdot 1\ [\text{mm}] \cdot 0.0025\ [\text{N/mm}] = 0.0004375\ [\text{N mm}]$. The released energy increment computed in each load step is shown in Fig. 12(a). The load parameter increment $\Delta\eta$ that represents the third independent variable, computed in each load step is presented in Fig. 12(b). Clearly, from Fig. 12, the problem presents energy dissipation even when the snap-back is produced (blue bars in Fig. 12(b)), showing that the energy release functional has a monotonically increasing nature. In Fig. 13 the amount of iterations needed for each load step in the numerical procedure is presented. From this figure, it can be concluded that for the proposed procedure, the average number of iterations per load step is half that needed by researchers, such as [19], for this *classical* example.

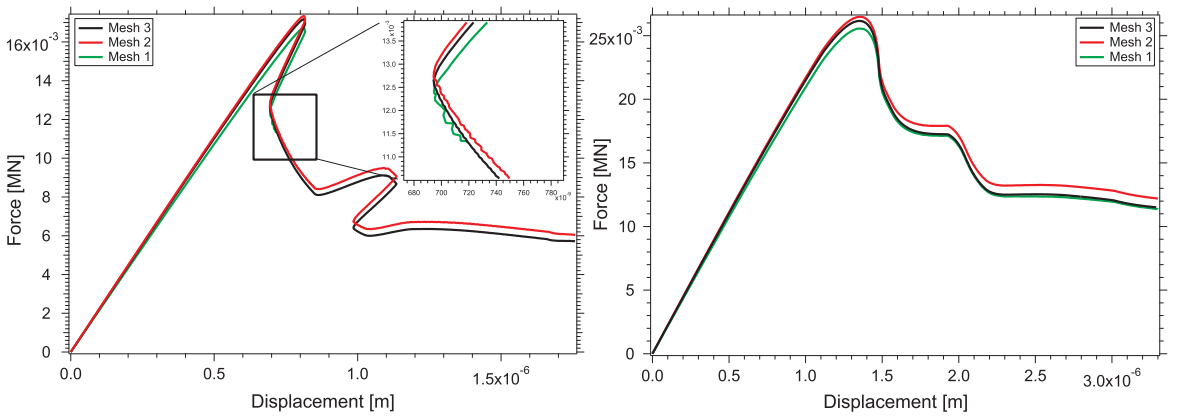

(a) Force-displacement curve for a fracture energy $G_c = 0.001 J/mm^2$. (b) Force-displacement curve for a fracture energy $G_c = 0.004 J/mm^2$.

Fig. 9. Mesh sensitivity analysis in unstable fractures controlled by energy dissipation.

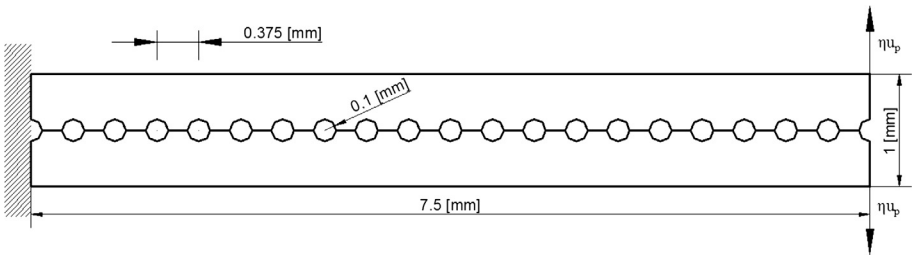

Fig. 10. Perforated double cantilever beam.

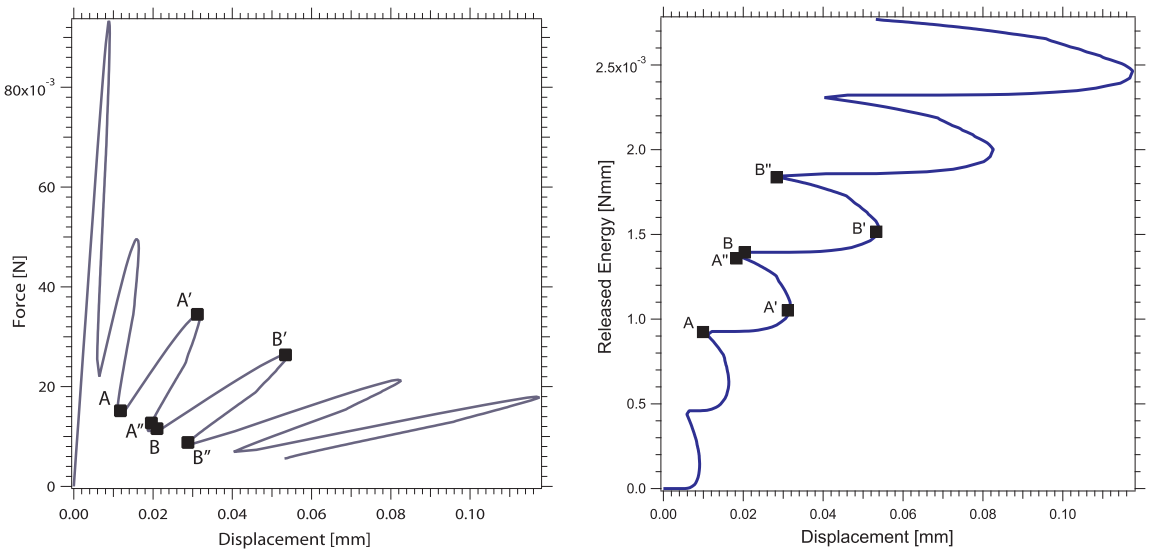

(a) Force versus displacement for $G_c = 0.0025$ N/mm . (b) Total released energy versus displacement for $G_c = 0.0025$ N/mm.

Fig. 11. Results for double cantilever beam in terms of total force and total released energy.

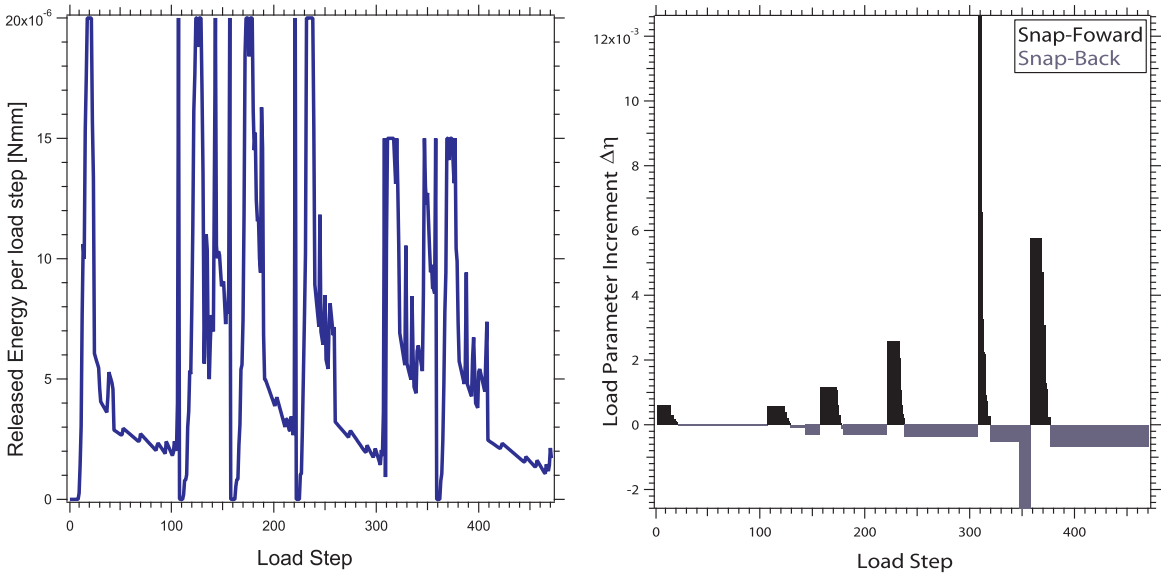

(a) Released energy rate in each load step for $G_c = 0.0025$ N/mm. (b) Load parameter η computed in each load step for $G_c = 0.0025$ N/mm.

Fig. 12. Results for double cantilever beam in terms of released energy per load step and the load parameter increment.

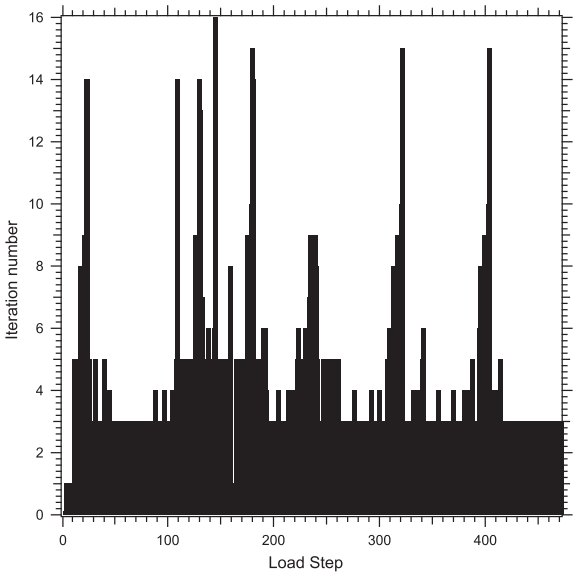

Fig. 13. Number of iterations in each load step.

4.4. Plate with hole

A square plate of 2000 [mm] side, with a non centered hole of 1000 [mm] diameter and two interfaces subjected to uniaxial tension is presented and analyzed. The objective of this example is to analyse the behaviour of the proposed method when different properties are used for the two interfaces. The geometry and boundary conditions of the problem are shown in Fig. 15. The value of the uniformly distributed force is $f_p = 1$ [N]. The elastic parameters used for bulk elements are $E = 20{,}000$ [MPa] for Young's modulus, $\nu = 0.2$ for Poison ratio, the ultimate stress is $\sigma_c = 3$ [MPa] and three different combinations of the fracture energy values are presented in Table 3. All cases correspond to a total released energy of 100 [N mm]. The plate is discretized by using 840 8-nodes quadrilateral (Q8) elements with nine gauss points for bulk and 2-nodes linear elements (L2) with two gauss points for the interface, with a total of 2756 nodes. The number of load steps needed to solve the problem is 920 for Case 1, 1224 for Case 2 and 740 for Case 3.

The stresses in the vertical direction for the analysed cases are presented in Fig. 16. The applied tension versus the vertical

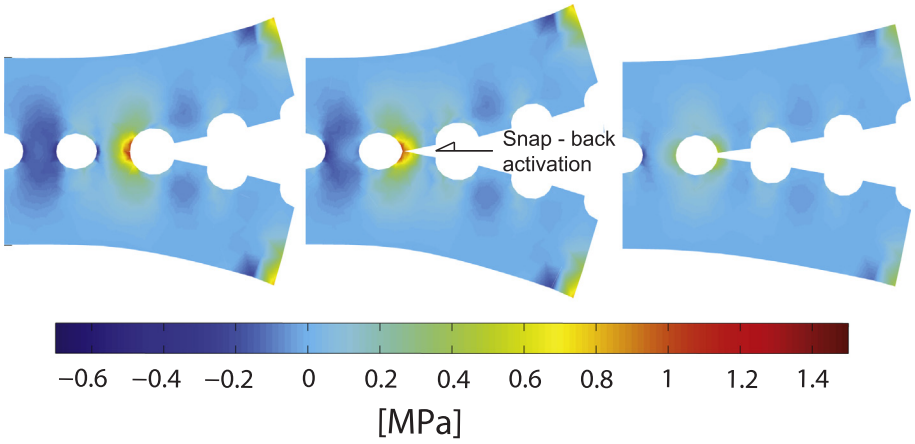

(a) Displacement and stress configuration for a double cantilever beam with G_c = 0.0025. Snapshots for points **A**,**A**' and **A**" in Fig. 11 (a).

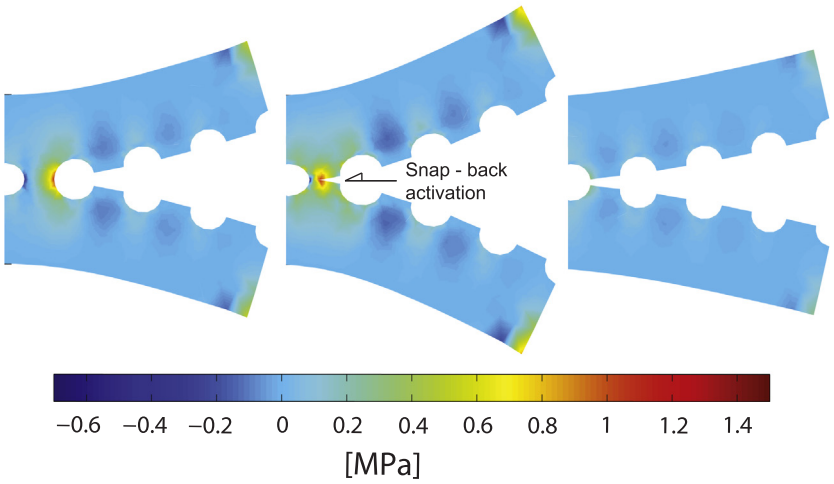

(b) Displacement and stress configuration for a double cantilever beam with G_c = 0.0025. Snapshots for points **B**,**B**' and **B**" in Fig. 11 (a)

Fig. 14. Vertical stress distribution in the double cantilever beam and snap-back activation.

displacement of point P and the variation of the total released energy are plotted in Fig. 17. The points where the instability stage starts are highlighted in Fig. 17(a) (Points A and B). It can be seen that for Case 1 and Case 3 the fracture modes are almost equivalent, with less energy dissipation in the second fracture stage (Fig. 17(b)). For Case 2, the fracture mode activated is quite different compared to the others for which, the crack propagation starts in the left interface. In this case, the instability stage is started in point A when the fracture advances in both interfaces. After that, due to the lower fracture energy, interface N°2 breaks down (Point B). Point C shows the last stage before the total rupture. The loading stage from point A′ in Fig. 17(b) is horizontal, showing that the the load stage does not imply energy release. A similar example can be found in Ref. [24], but different combinations of material fracture properties are used in this paper, showing the ability of the proposed method to deal with this context. The total released energy variation during the damage process exhibits that the curve asymptotically approaches to the total energy of 100 [N mm], with a continuous decrease of the load parameter. This could be a limitation of the method because the total damage of the sample can never be reached.

5. Concluding remarks

A computational fracture method based on an augmented Lagrangian functional equipped with an energy-released control has been formulated, discretizated and discussed. The proposed path following strategy shows the ability to compute the equilibrium path using a scalar parameter with a physical meaning (released energy) as control variable. The proposed approach is able to deal with fracture problems even when the crack path is a priori unknown and presents a good performance in the context of mixed

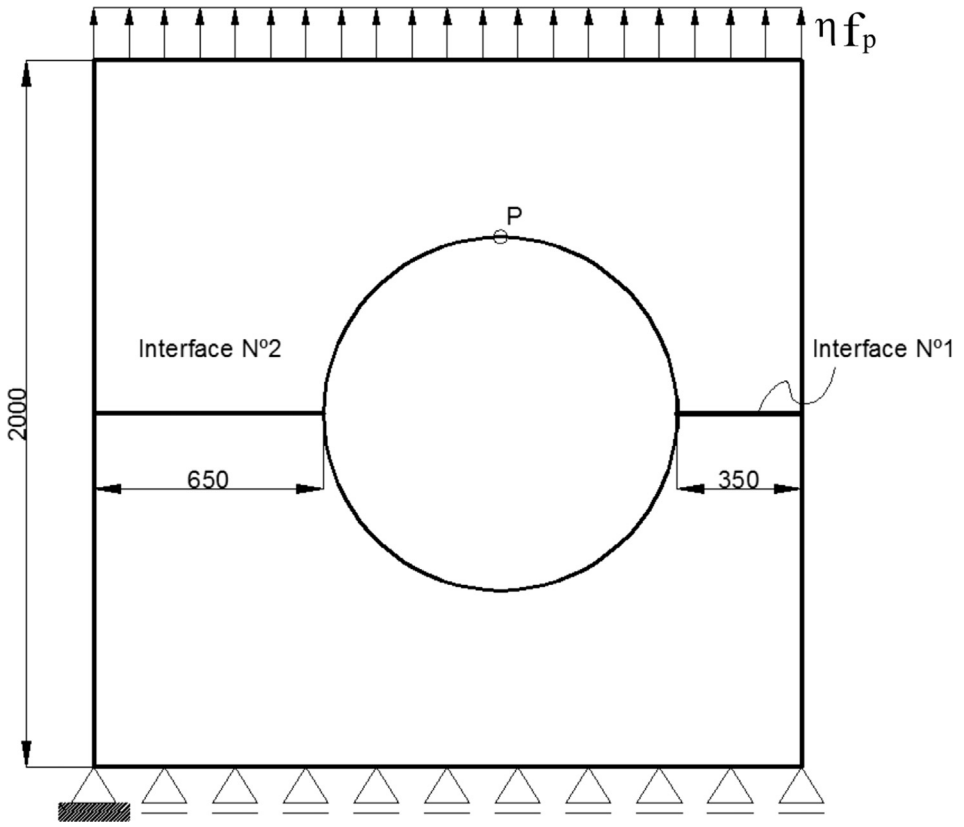

Fig. 15. Plate with hole.

Table 3
Material properties for plate with hole.

	Interface mat. N^o 1	Interface mat. N^o 2
Case 1	$G_c = 0.1$ [N/mm]	$G_c = 0.1$ [N/mm]
Case 2	$G_c = 0.15$ [N/mm]	$G_c = 0.073$ [N/mm]
Case 3	$G_c = 0.05$ [N/mm]	$G_c = 0.127$ [N/mm]

formulations. The proposed constraint equation $\mathscr{G}_3$ maintains a variational consistency, resulting in a method with a straightforward implementation in a classical Newton-Raphson scheme.

Several examples with abrupt crack propagation were presented, including a discussion about the interpolation order in the Lagrangian field and the presence of spurious energy release in elastic regime. It was proved that an optimal interpolation in the Lagrangian field is mandatory to avoid spurious dissipations and it depends on the structural configuration. For tortuous fractures the discrete spaces for the finite elements are $\mathscr{X}^h = \mathscr{P}_d^1(\Gamma^h)$, while for the case of fiber-matrix debonding they are $\mathscr{X}^h = \mathscr{P}_c^2(\Gamma^h)$. Using a simple example based on a polycrystal topology undergoing an inter-granular fracture mechanism, the dependence of the released energy functional on the mesh density was discussed. An intermittent snap-back is observed for coarse meshes due to the cohesive length of the cohesive law not being resolved within the size of the considered elements. A smoother response is obtained when the fracture energy is increased or the mesh is refined. A perforated double cantilever beam and a plate with a non centered hole combining different fracture properties were presented and analyzed. In those examples, the model shows the ability to efficiently control and compute the response of different types of cracks, including snap back phenomena with mixed fracture properties. The analysis of this type of problem constitutes an original result in the bibliography. The hypothesis of monotonically increasing released energy stated to formulate the path-following functional is verified in the presented examples. Another important feature of the presented method is that it can accurately capture the total energy that the interfaces are capable of dissipating. In some cases, as in the last example, this limit value is asymptotically reached. In the double cantilever beam example, it was shown that a negative load parameter does not implies an artificial unloading, but it can involve energy dissipation. The analysis of the method ability to treat problems related to composites materials with diffusive failure, dynamic fracture and more complex traction separation laws is left for future works.

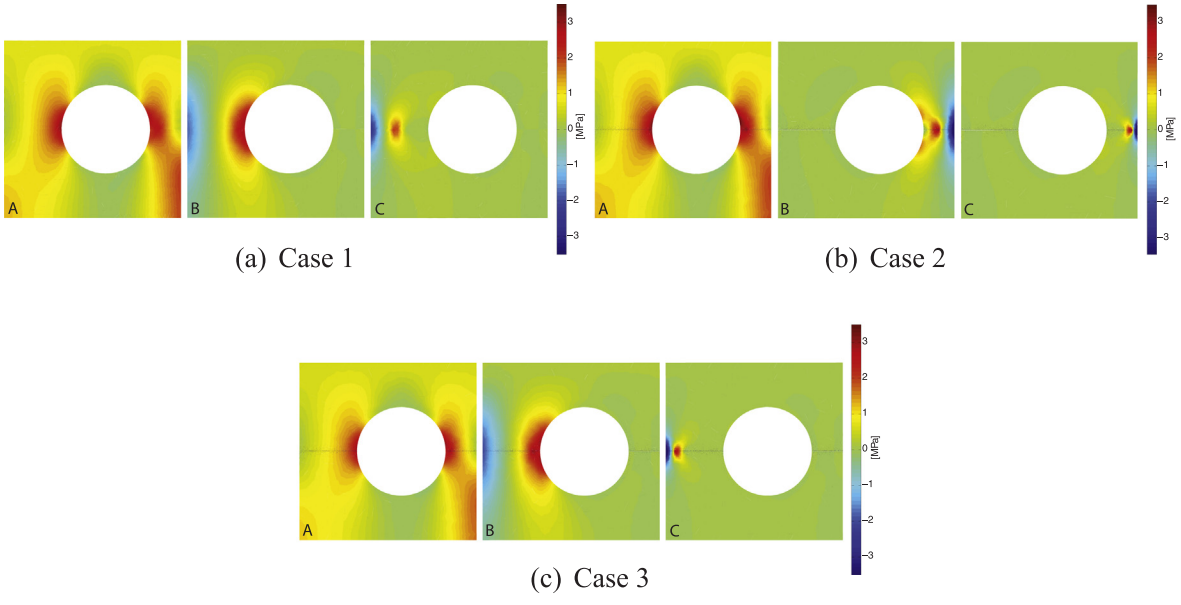

Fig. 16. Stress in vertical direction σ_y.

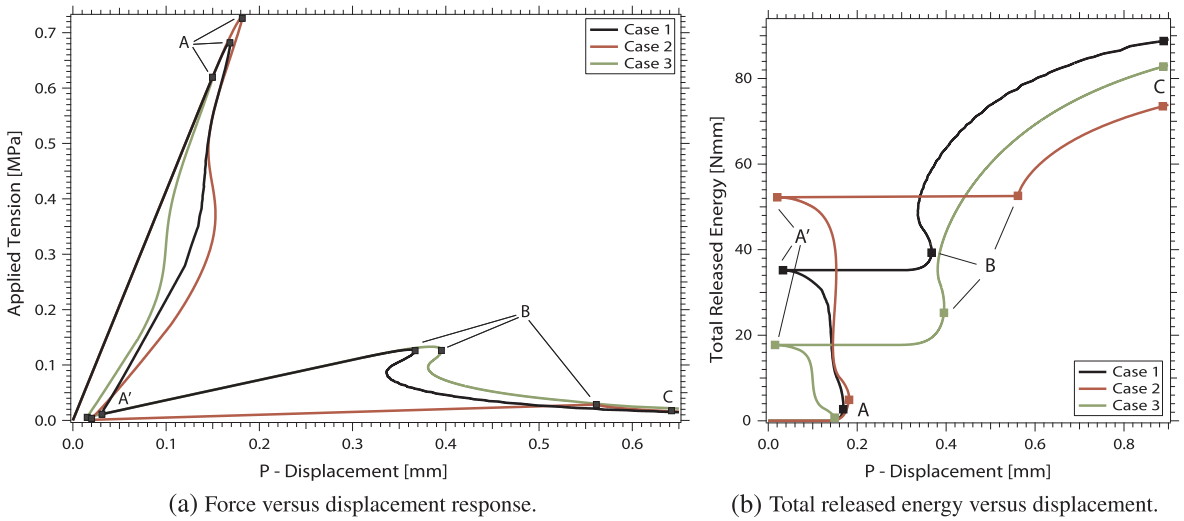

Fig. 17. Results for the plate with a hole.

Acknowledgements

The authors wish to thank the financial support of National Agency for Scientific and Technological Promotion (PICT 2013 1740), National Scientific and Technological Research Council (CONICET) and National University of Tucumán research Council (PIUNT 26E/520). The work of S.M. Giusti was partially supported by the European Research Council under the European Unions Seventh Framework Programme (FP/2007-2013)/ERC Grant Agreement n. 320815 (ERC Advanced Grant Project “Advanced tools for computational design of engineering materials” COMP-DES-MAT).

Appendix A. Supplementary material

Supplementary data associated with this article can be found, in the online version, at http://dx.doi.org/10.1016/j.engfracmech.2018.03.004.

References

[1] Pohl T, Ramm E, Bischoff M. Adaptive path-following schemes for problems with softening. Fin Elem Anal Des 2014;86:12–22.
[2] Wempner GA. Discrete approximations related to non-linear theories of solids. Int J Solids Struct 1971;7:1581–99.
[3] Riks E. An incremental approach to the solution of snapping and buckling problems. Int J Solids Struct 1979;15:529–51.
[4] Ramm E. Strategies for tracing the non-linear response near limit points. In: Non-linear finite element analysis in structural mechanics. Berlin: Springer; 1981.
[5] Crisfield MA. A fast incremental/iterative solution procedure that handles snap-through. Comput Struct 1981;13:55–62.
[6] Crisfield MA. Local instabilities in the non-linear analysis of reinforced concrete beams and slabs. Inst Civ Eng Proc 1982;73:135–45.
[7] de Borst R. Computation of post-bifurcation and post-failure behavior of strain-softening solids. Comput Struct 1987;25:211–24.
[8] Gutierrez MA. Energy release control for numerical simulations of failure in quasi-brittle solids. Commun Numer Methods Eng 2004;20:19–29.
[9] Verhoosel CV, Remmers JC, Gutierrez MA. A dissipation-based arc-length method for robust simulation of brittle and ductile failure. Int J Numer Methods Eng 2009;77:1290–321.
[10] May S, Vignollet J, de Borst R. A new arc-length control method based on the rates of the internal and the dissipated energy. Eng Comput: Int J Comput-Aided Eng Softw 2016;33:100–15.
[11] May S, de Borst R, Vignollet J. PowellSabin B-splines for smeared and discrete approaches to fracture in quasi-brittle materials. Comput Methods Appl Mech Eng 2016;307:193–214.
[12] Singh N, Verhoosel CV, de Borst R, van Brummelen EH. A fracture-controlled path-following technique for phase-field modeling of brittle fracture. Fin Elem Anal Des 2016;113:14–29.
[13] Lorentz E. A mixed interface finite element for cohesive zone models. Comput Methods Appl Mech Eng 2008;198:302–17.
[14] Elguedj T, Gravouil A, Combescure A. A mixed augmented Lagrangian-extended finite element method for modelling elasticplastic fatigue crack growth with unilateral contact. Int J Numer Methods Eng 2007;71:1569–97.
[15] Sadaba S, Romero I, Gonzalez C, Llorca J. A stable X-FEM in cohesive transition from closed to open crack. Int J Numer Meth Eng 2015;101:540–70.
[16] Baiges J, Codina R, Henke F, Shahmiri S, Wall WA. A symmetric method for weakly imposing Dirichlet boundary conditions in embedded finite element meshes. Int J Numer Meth Eng 2012;90:636–58.
[17] Labanda NA, Giusti SM, Luccioni BM. Meso-scale fracture simulation using an augmented Lagrangian approach. Int J Damage Mech 2018;27(1):138–75.
[18] Verhoosel CV, Gutiérrez MA. Modelling inter- and transgranular fracture in piezoelectric polycrystals. Eng Fract Mech 2009;76:742–60.
[19] Nguyen VP, Nguyen-Xuan H. High-order B-splines based finite elements for delamination analysis of laminated composites. Compos Struct 2013;102:261–75.
[20] Ladevèze P. Nonlinear computational structural mechanics. In: New approaches and non-incremental methods of calculation. New York: Springer-Verlag; 1999.
[21] Allix O, Ladevèze P, Gilletta D, Ohayon R. A damage prediction method for composite structure. Int J Numer Methods Eng 1989;27:271–83.
[22] Boisse P, Bussy P, Ladevèze P. A new approach in non-linear mechanics: the large time increment method. Int J Numer Methods Eng 1990;29:647–63.
[23] Vandoren B, De Proft K, Simone A, Sluys LJ. A novel constrained LArge Time INcrement method for modelling quasi-brittle failure. Comput Methods Appl Mech Eng 2013;265:148–62.
[24] Lorentz E, Badel P. A new path-following constraint for strain-softening finite element simulations. Int J Numer Methods Eng 2004;60:499–526.
[25] Fortin M, Glowinski R. Augmented Lagrangian methods: application to the numerical solution of boundary-value problems. North-Holland – studies in mathematics and its applications; 1983.
[26] Talischi C, Paulino G, Pereira A, Menezes I. PolyMesher: a general-purpose mesh generator for polygonal elements written in Matlab. Struct Multidiscip Optim 2012;45:309–28.
[27] Clarke Frank H. Non smooth analysis and optimization. New York: John Wiley and Sons; 1983.
[28] Turon A, Davila CG, Camanho PP, Costa J. An engineering solution for mesh size effects in the simulation of delamination using cohesive zone models. Eng Fract Mech 2007;74:1665–82.
[29] Harper PW, Hallett SR. Cohesive zone length in numerical simulations of composite delamination. Eng Fract Mech 2007;75(16):4774–92.